Supplement Material for "Observed modulation of wintertime Western Arctic mixed-phase cloud properties by sea ice conditions, their long-term variabilities and trends"

Pablo Saavedra Garfias and Heike Kalesse-Los

July 4, 2025

S1 Climatology of sea ice around the NSA site

S1.1 Yearly distribution of sea ice concentration

Here we highlight the conceptual difference between the sea ice conditions within a 50 km radius semi-circle around NSA site and the sea ice conditions utilized to apply the PSG23 method (Sec. 2.4). In Fig. S1 the distribution (normalized relative to the mode, i.e. the y-axis represents the most frequent SIC bin when equal to one) of two statistics are shown: the average sea ice concentration corresponding to the whole 50 km semi-circle $SIC_{\odot}$ (red bars), and the average for only SIC within the $\pm 3°$ conical sector (grey bars). Conceptually these two quantities are different, with the $SIC_{\odot}$ not changing with time (AMSR2 standard SIC daily observations), while the second average changes dynamically as a function of maximum $\nabla_z \texttt{WVT}$ with one minute temporal resolution (same temporal resolution as the synergistic dataset in Sec. 2.2). From Fig. S1 it can be seen that for every wintertime the sea ice condition features a multi-modal distributions which is an indicator for variability of the ocean's thermodynamics regime during the period from November to April. A particularly high occurrence of low $SIC_{\odot}$ values (e.g. $<40\%$ for red bars in Fig. S1) is observed during the winters 2012/13, 2016/17, 2017/18, 2019/20, 2023/24, 2024/25, which contrasts to other years where $SIC_{\odot}$ barely shows values below 60% as expected for wintertime. On the other hand, the distributions of SIC as a function of maximum $\nabla_z \texttt{WVT}$ (grey bars in Fig. S1), do not generally resemble the 50 km semi-circle $SIC_{\odot}$ distributions, with most of the occurrences happening above 80%. Contrary to the fact that a randomly selected conical sector of AMSR2 sea ice cells should resemble the $SIC_{\odot}$ distribution, Fig. S1 supports the ability of the WVT

to physically separate the sea ice conditions around NSA site and to dynamically link certain sea ice states along the WVT path to the observed clouds above NSA site.

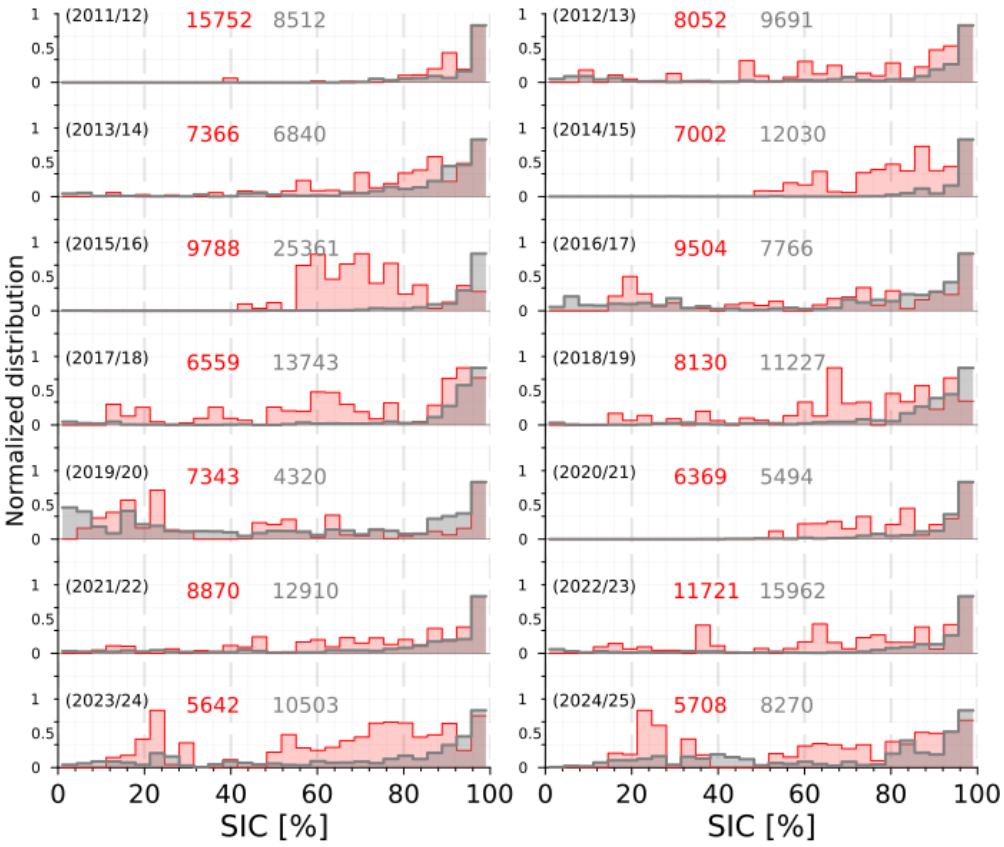

Figure S1: Normalized distribution of mean SIC within a 50 km semi-circle centred at NSA (red bars) and within the ±3° conical sector aligned to the direction of maximum WVT (grey bars) for wintertime from 2011 to 2024. The corresponding wintertime is indicated in parenthesis e.g. from November 2012 to April 2013 as (2012/13). The most frequent SIC bin is assigned to 1 in the y-axis and its value in number of observations is shown by the red and grey numbers.

S2 Time series of MPC properties

S2.1 Method i: Trends by moving average method

Results related to the Sec. 3.2.1 are shown in the following. In Fig. S2 the ice water path (IWP) is shown in panels (a) and (b), the ice particles effective radius r_{eff} in panels (c) and (d), and the cloud layer depth in panels (e) and (f).

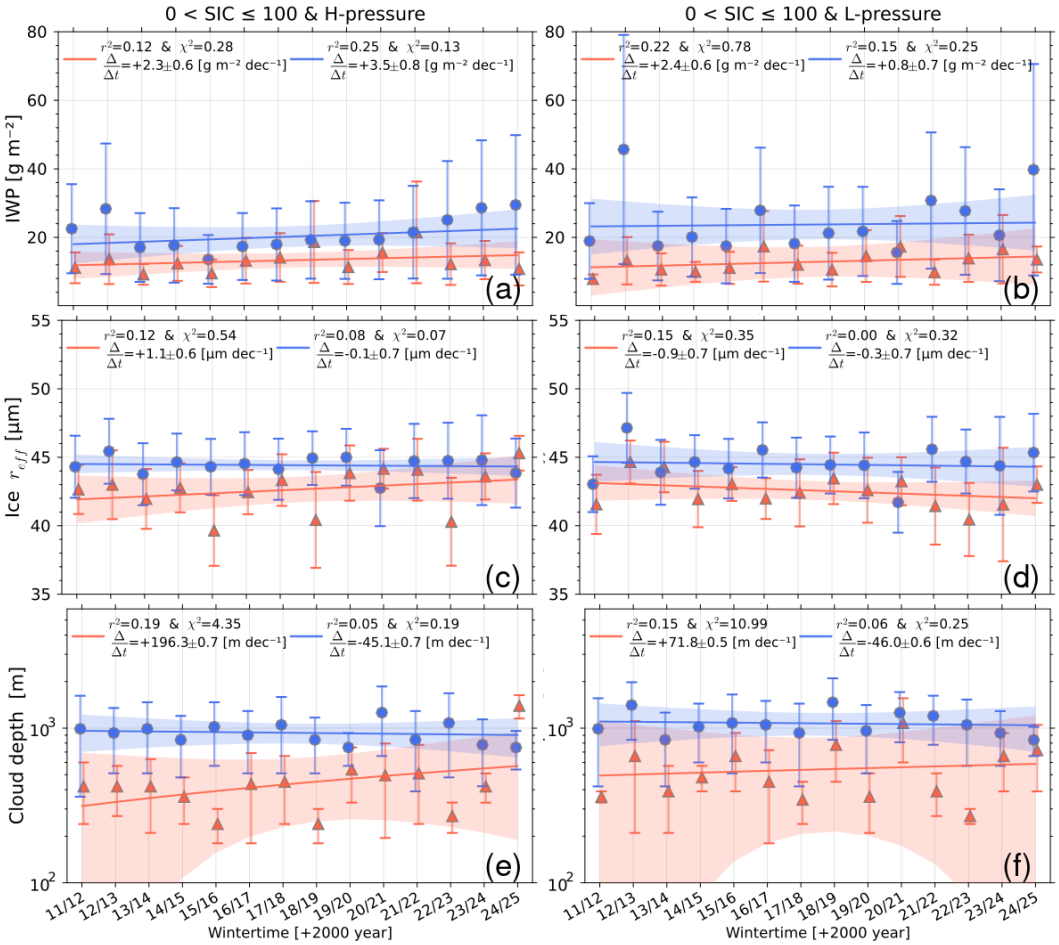

Figure S2: MPC time series for coupled (blue circles) and decoupled (orange triangles) represented by the median ($\mu_{1/2}$) and σ_{mad} (bars) of wintertime distributions. H-pressure (left column) and L-pressure (right column) for IWP (a, b), ice r_{eff} (c, d), and cloud layer depth δ_h (e, f). The linear trends (± uncertainty) are indicated with the solid lines (shared area is 95% CI) and trend values in units per decade, the coefficient of determination r^2, and χ^2 are presented in legend.

Additional results are shown in Fig. S3 for droplet effective radius r_{eff} in panels (a) and (b), surface skin temperature T_{skin} in panes (c) and (d), and cloud layer temperature

lapse-rate in panels (e) and (f).

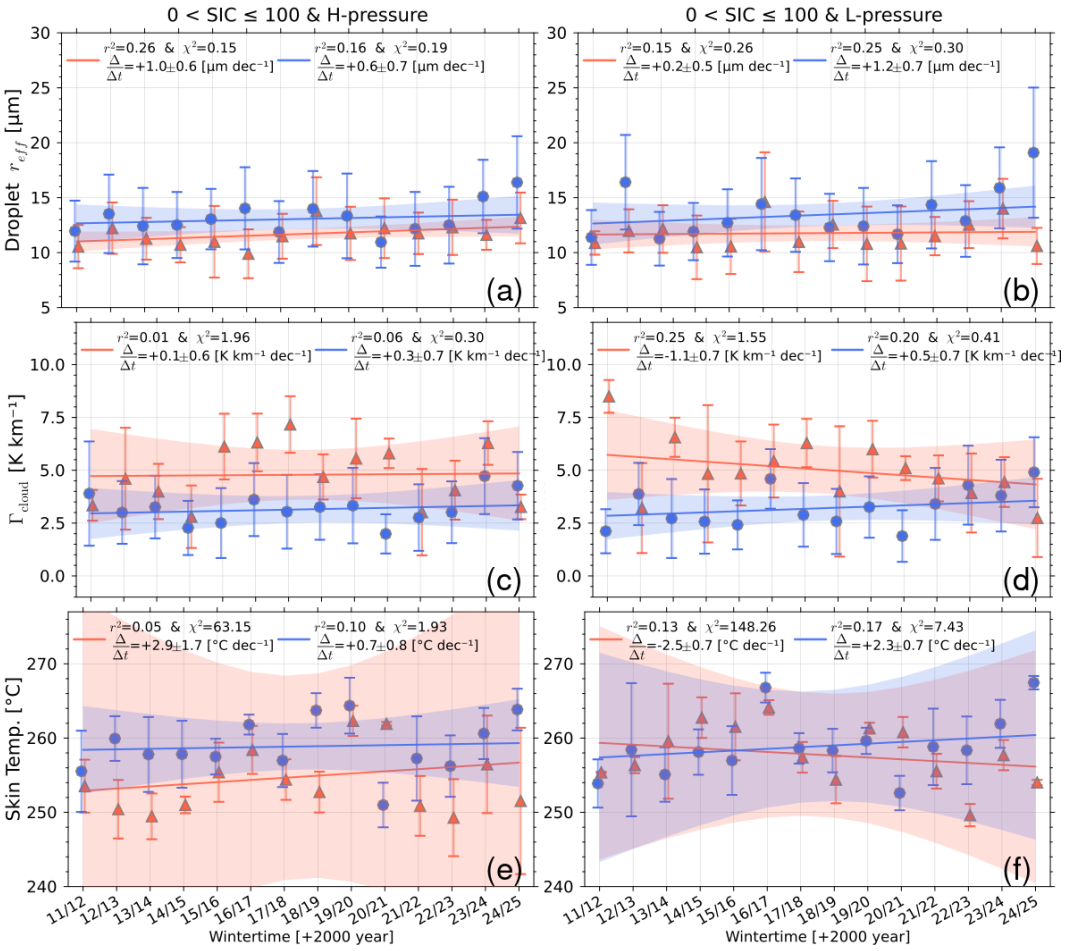

Figure S3: Same as in Fig. S2 for liquid droplet effective radius r_{eff} (a, b), cloud layer temperature lapse-ratio Γ_{cloud} (c, d), and surface skin temperature (e, f). The linear trends (± uncertainty) are indicated with the solid lines (shared area is 95% CI) and trend values in units per decade, the coefficient of determination r^2, and χ^2 are presented in legend.

S2.2 Method ii: Trends by periodic analysis method

This section contains additional results for Sec. 3.2.2 regarding MPC variables like: ice water path (IWP), ice effective radius r_{eff}, and cloud layer depth δ_h, for H-pressure in Fig. S4 and for L-pressure in Fig. S5.

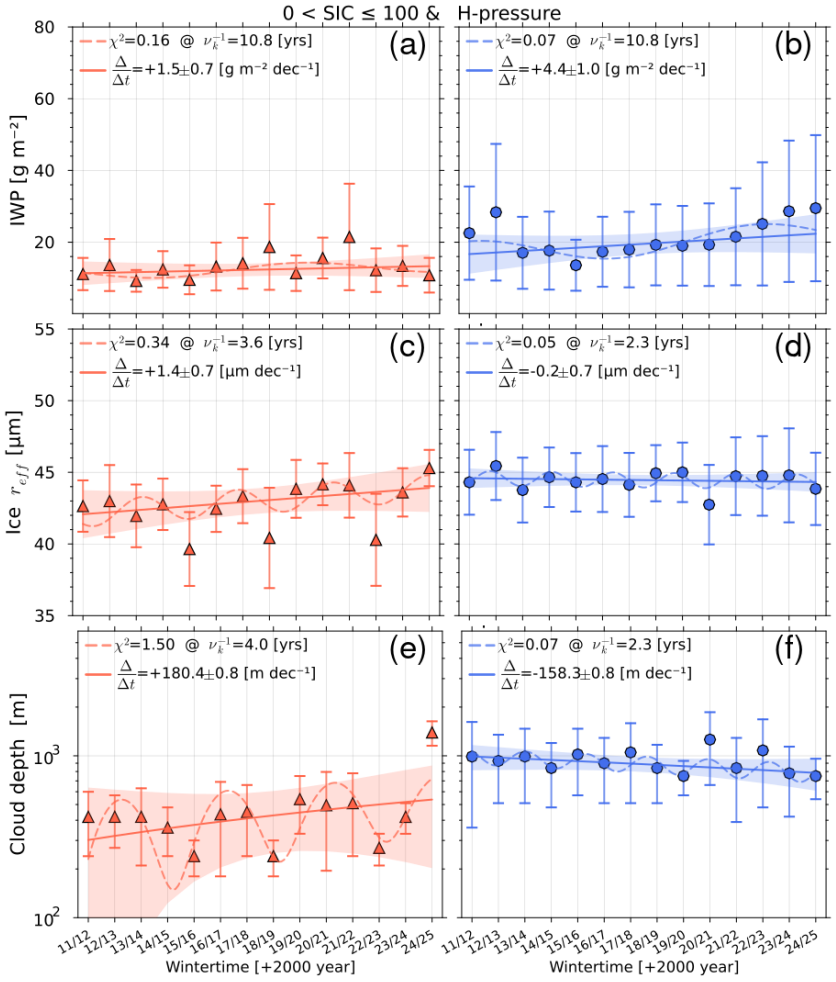

Figure S4: Time series for H-pressure systems with IWP (a) and (b), ice r_{eff} (c, d), and δ_h (e, f). Left column panels (a, c, e) shown decoupled (orange triangles) cases and right column (b, d, f) are coupled (blue circles). The best fit curves are dashed-lines and linear trends are indicated with the solid lines (shared area is 95% CI).

The droplet effective radius r_{eff}, cloud layer lapse-rate, and surface skin temperature are shown for H-pressure in Fig. S6 and for L-pressure in Fig. S7.

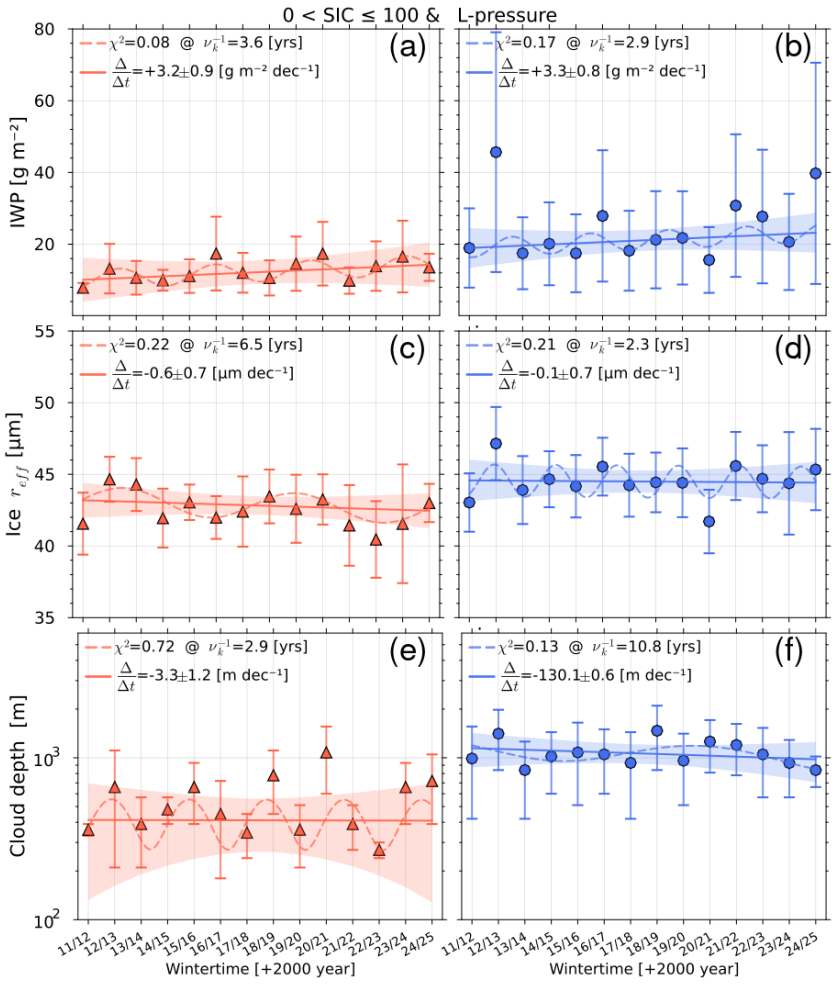

Figure S5: Same as Fig. S4 but for L-pressure systems.

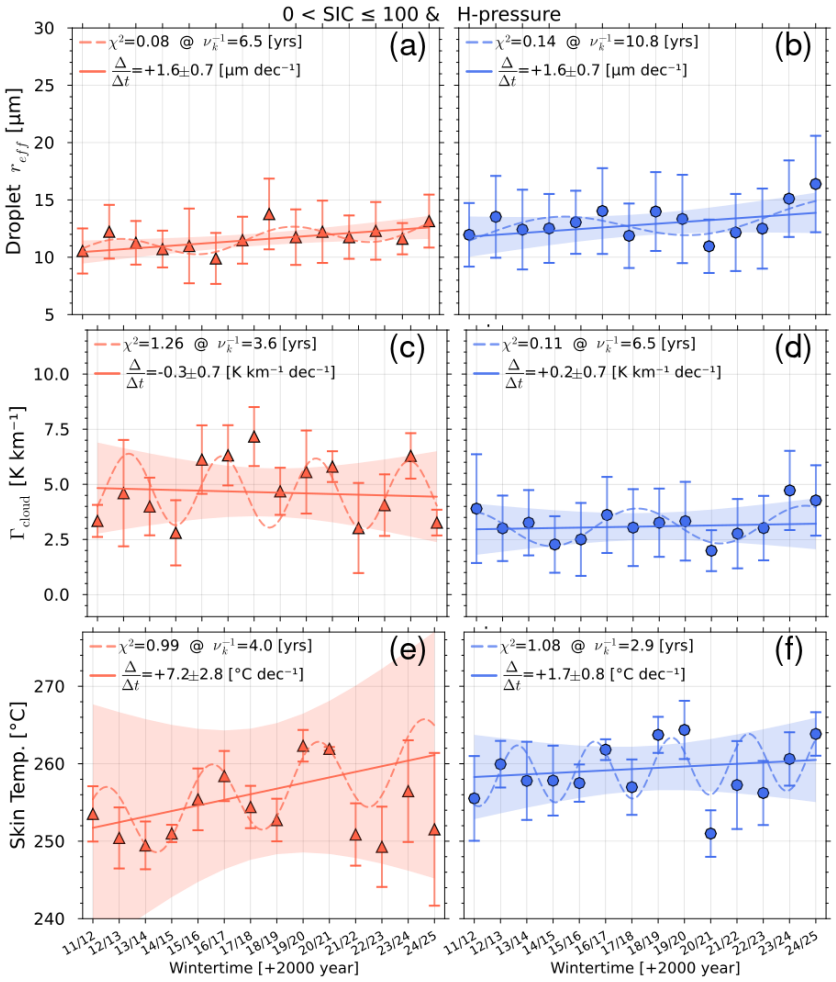

Figure S6: Time series for H-pressure systems with droplet r_{eff} (a) and (b), Γ_{cloud} (c, d), and T_{skin} (e, f). Left column panels (a, c, e) shown decoupled (orange triangles) cases and right column (b, d, f) are coupled (blue circles). The best fit curves are dashed-lines and linear trends are indicated with the solid lines (shared area is 95% CI).

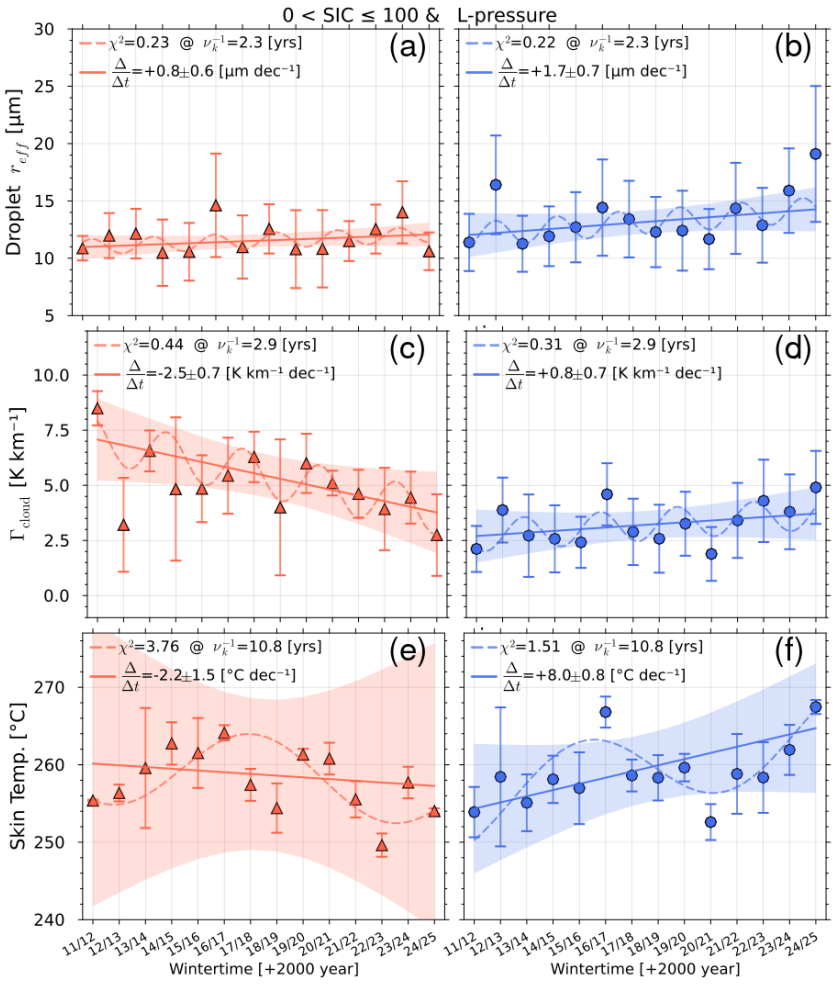

Figure S7: Same as Fig. S6 but for L-pressure systems.

S2.3 Time series for the lower/upper 50th percentile SIC decomposition

Results for the time series decomposition of trend analysed by method *ii* discussed in main document results in Sec. 3 and appendix B1 but for L-pressure systems (Fig. S8). Same for T_{skin} H-pressure systems in Fig. S9. The summary of trends as a function of SIC is discussed in the main document Sec. 3 and appendix B2.

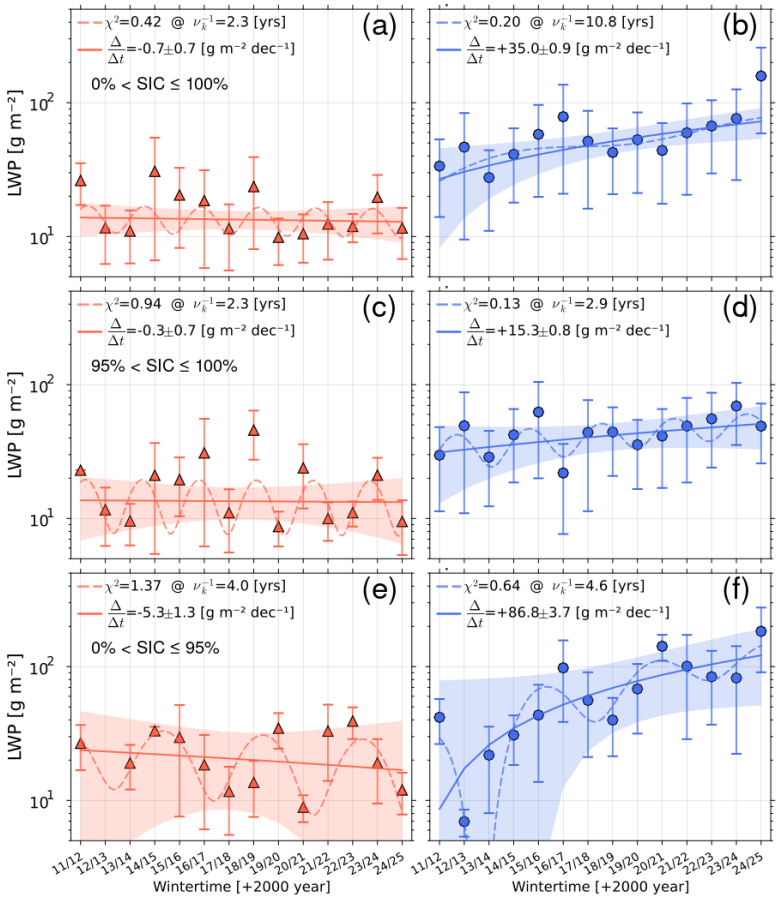

Figure S8: Time series of T_{skin} for coupled and decoupled cases under H-pressure systems. The time series are decomposed by the range of SIC: (a) and (b) all SIC considered, (c) and (d) for SIC $>$ 95% and SIC $\leq$ 100%, and (e) and (f) for SIC $>$ 0% and SIC $\leq$ 95%.

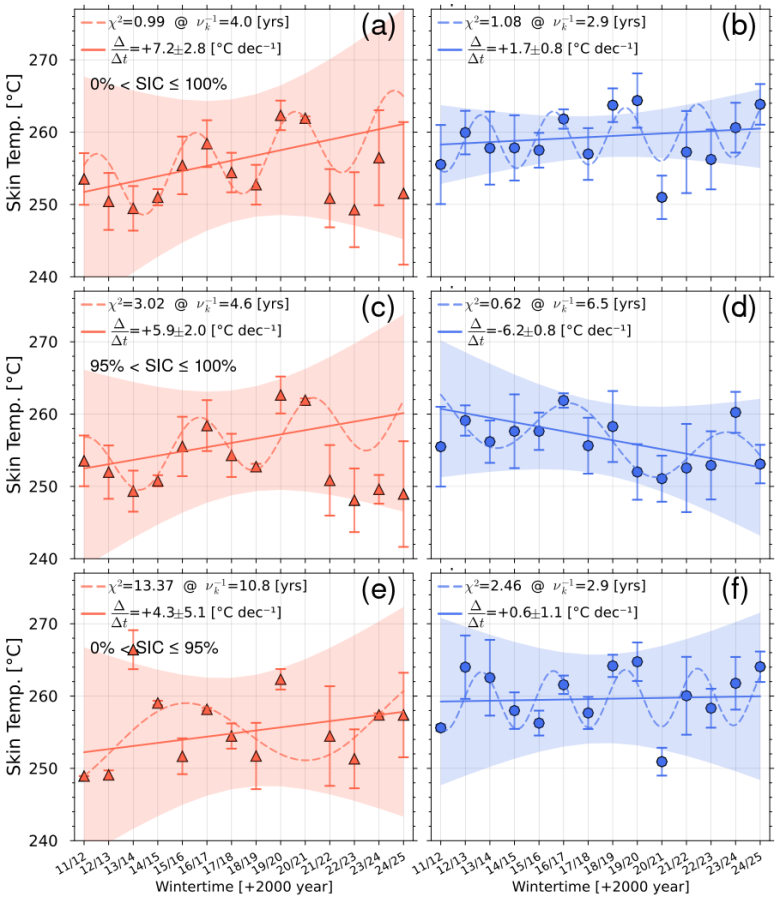

Figure S9: Time series of T_{skin} for coupled and decoupled cases under H-pressure systems. The time series are decomposed by the range of SIC: (a) and (b) all SIC considered, (c) and (d) for SIC $>$ 95% and SIC $\leq$ 100%, and (e) and (f) for SIC $>$ 0% and SIC $\leq$ 95%.

S3 Data Availability

The daily data availability for the instrumentation (Table 1 in Sec. 2.1) and retrieval products needed for the study is visualized in S10. Note that for CloudNet to be able to characterize the clouds, data labelled as 1, 2, 3, and 6 (alternative 4) are needed; to apply the PSG23 method all data are necessary.

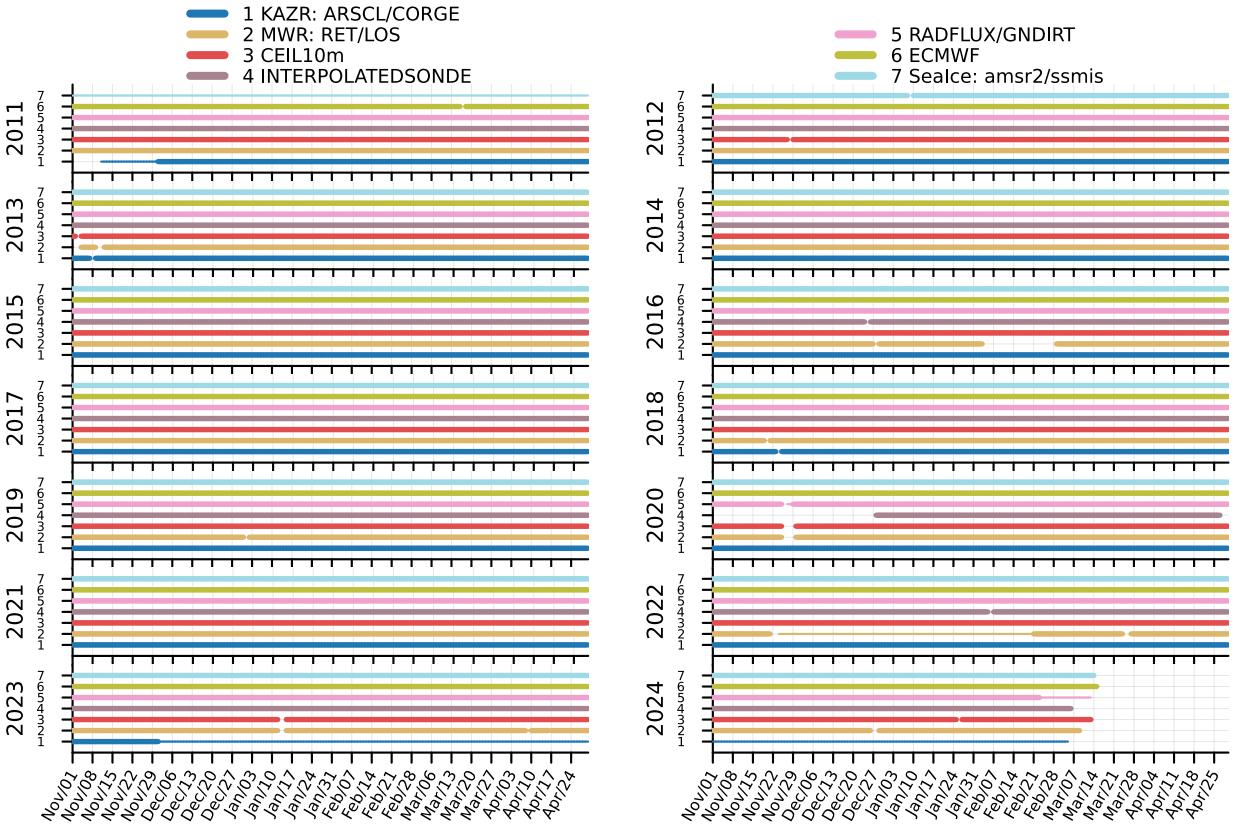

Figure S10: Daily data availability during fourteen wintertime periods for NSA site instrumentation, as in Table 1, required to characterize and estimate the cloud and sea ice properties. Gaps in the time-lines show when no data product is available. Thinner lines indicate the use of alternative product highlighted at the left of / in top legend and marked as ⋆ in Table 1.